



UNIVERSITY OF LEEDS

This is a repository copy of *Deposition pattern and tracer particle motion of evaporating multi-component sessile droplets*.

White Rose Research Online URL for this paper:  
<http://eprints.whiterose.ac.uk/118952/>

Version: Accepted Version

---

**Article:**

Amjad, M, Yang, Y, Raza, G et al. (5 more authors) (2017) Deposition pattern and tracer particle motion of evaporating multi-component sessile droplets. *Journal of Colloid and Interface Science*, 506. pp. 83-92. ISSN 0021-9797

<https://doi.org/10.1016/j.jcis.2017.07.025>

---

© 2017 Elsevier Inc. This manuscript version is made available under the CC-BY-NC-ND 4.0 license <http://creativecommons.org/licenses/by-nc-nd/4.0/>

**Reuse**

Items deposited in White Rose Research Online are protected by copyright, with all rights reserved unless indicated otherwise. They may be downloaded and/or printed for private study, or other acts as permitted by national copyright laws. The publisher or other rights holders may allow further reproduction and re-use of the full text version. This is indicated by the licence information on the White Rose Research Online record for the item.

**Takedown**

If you consider content in White Rose Research Online to be in breach of UK law, please notify us by emailing [eprints@whiterose.ac.uk](mailto:eprints@whiterose.ac.uk) including the URL of the record and the reason for the withdrawal request.



[eprints@whiterose.ac.uk](mailto:eprints@whiterose.ac.uk)  
<https://eprints.whiterose.ac.uk/>

## Accepted Manuscript

Deposition pattern and tracer particle motion of evaporating multi-component sessile droplets

Muhammad Amjad, Yang Yang, Ghulam Raza, Hui Gao, Zhang Jun, Leping Zhou, Xiaoze Du, Dongsheng Wen

PII: S0021-9797(17)30792-0  
DOI: <http://dx.doi.org/10.1016/j.jcis.2017.07.025>  
Reference: YJCIS 22554

To appear in: *Journal of Colloid and Interface Science*

Received Date: 29 May 2017  
Revised Date: 6 July 2017  
Accepted Date: 7 July 2017

Please cite this article as: M. Amjad, Y. Yang, G. Raza, H. Gao, Z. Jun, L. Zhou, X. Du, D. Wen, Deposition pattern and tracer particle motion of evaporating multi-component sessile droplets, *Journal of Colloid and Interface Science* (2017), doi: <http://dx.doi.org/10.1016/j.jcis.2017.07.025>

This is a PDF file of an unedited manuscript that has been accepted for publication. As a service to our customers we are providing this early version of the manuscript. The manuscript will undergo copyediting, typesetting, and review of the resulting proof before it is published in its final form. Please note that during the production process errors may be discovered which could affect the content, and all legal disclaimers that apply to the journal pertain.



# Deposition pattern and tracer particle motion of evaporating multi-component sessile droplets

Muhammad Amjad<sup>1,2</sup>, Yang Yang<sup>3</sup>, Ghulam Raza<sup>1</sup>, Hui Gao<sup>1</sup>, Zhang Jun<sup>4</sup>, Leping Zhou<sup>3</sup>, Xiaoze Du<sup>3</sup>  
Dongsheng Wen<sup>4,1\*</sup>

<sup>1</sup>School of Chemical and Process Engineering, University of Leeds, Leeds, LS2 9JT, UK

<sup>2</sup>Department of Mechanical, Mechatronics and Manufacturing Engineering (KSK Campus), University of Engineering and Technology Lahore, Pakistan.

<sup>3</sup>School of Energy, Power and Mechanical Engineering, North China Electric University, Beijing 102206, P.R. China.

<sup>4</sup>School of Aeronautic Science and Engineering, Beihang University, Beijing, 100191, P.R. China

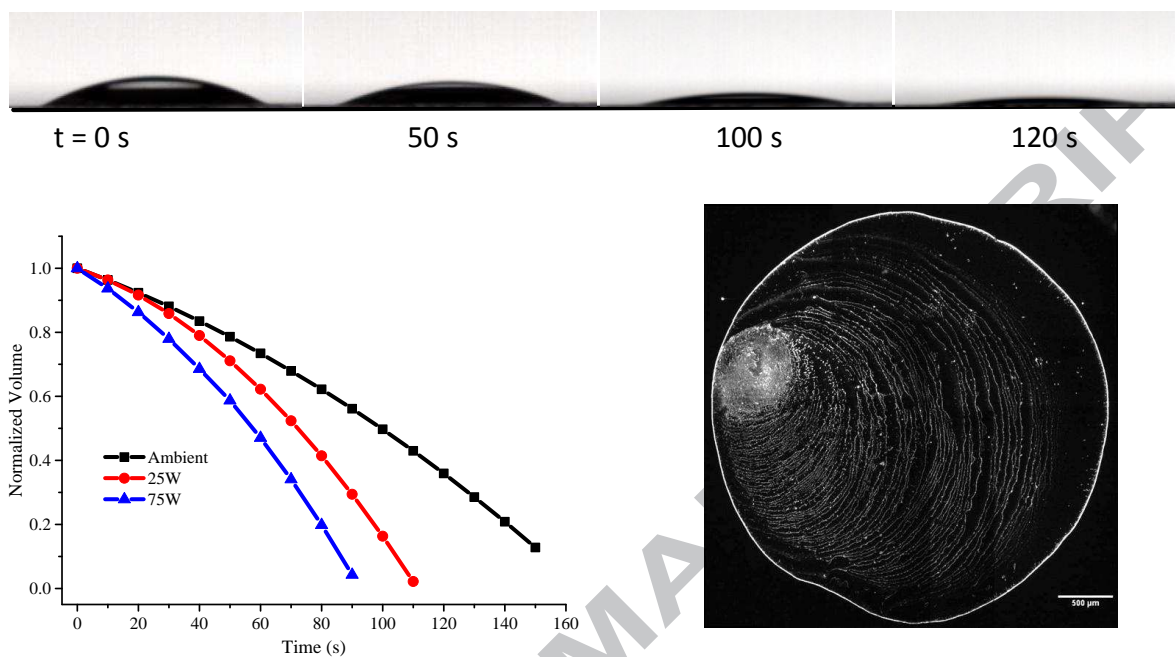
**Abstract:** The understanding of near-wall motion, evaporation behavior and dry pattern of sessile nanofluid droplets is fundamental to a wide range of applications like painting, spray drying, thin film coating, fuel injection and inkjet printing. However, a deep insight into the heat transfer, fluid flow, near-wall particle velocity and their effects on the resulting dry patterns is still much needed to take the full advantage of these nano-sized particles in the droplet. This work investigates the effect of direct absorptive silicon/silver (Si/Ag) hybrid nanofluids via two experiments. The first experiment identifies the motion of tracer particles near the triple line of a sessile nanofluid droplet on a super-hydrophilic substrate under ambient conditions by the multilayer nanoparticle image velocimetry (MnPIV) technique. The second experiment reveals the effect of light-sensitive Si/Ag composite nanoparticles on the droplet evaporation rate and subsequent drying patterns under different radiation intensities. The results show that the presence of nanoparticle in a very small proportion significantly affects the motion of tracer particles, leading to different drying patterns and evaporation rates, which can be very important for the applications such as spray coating and inkjet printing.

---

\*Corresponding author: Email: [d.wen@buaa.edu.cn](mailto:d.wen@buaa.edu.cn)

Phone: +44-113-3432678

## Graphical abstract



## Keywords

Dry pattern, droplet evaporation, nanofluid, total internal reflection, direct absorption

## 1. Introduction

Liquid droplet evaporation has a wide range of applications such as inkjet printing, thin film coating, spray drying, fuel injection and optoelectronic device manufacturing [1-4], as well as the diagnosis of diseases from drying the blood droplet and DNA microchips [5-7]. The deposition pattern of a droplet depends on the fluid flow within the droplet [8-13], temperature gradient [9, 14, 15], concentration and type of the nanoparticles [16-18]. The nature of the substrate [19-23] and type of base fluid [24, 25] also have important roles on the formation of droplet deposition patterns. The fluid flow within a nanofluid based droplet during evaporation can either be a capillary flow or Marangoni flow. When the peripheral walls of the droplet are pinned on the substrate surface at solid-liquid-vapor interface, also called three phase line or triple line, liquid flows radially outward to refill the liquid loss due to evaporation, which is known as capillary flow [12]. Marangoni flow, on the contrary, works with a reverse direction and due to non-uniformly distributed surface tension alongside the liquid-vapor line. This uneven distribution of surface tension may either be due to the temperature gradient [14, 15] or concentration gradient [12, 26].

The effect of various types of nanoparticles on the evaporation of a droplet has been investigated in many studies [16-18]. Gan et al. [16] studied the evaporation rate of ethanol based  $\text{Al}_2\text{O}_3$  and Al nanofluid at various radiation levels, and showed that the evaporation rate of Al nanofluid was better than that of  $\text{Al}_2\text{O}_3$  due to a higher absorption of Al nanoparticles. The effect of adding laponite,  $\text{Fe}_2\text{O}_3$  and Ag nanoparticles to deionized water was investigated by Chen et al. [17] in terms of nanofluid droplet evaporate rate. The evaporation rate constants for nanofluids were found to be different from the classical  $d^2$ -law. While Ag enhanced the evaporation rate, laponite and  $\text{Fe}_2\text{O}_3$  particles were found to suppress it, which was ascribed to the apparent heat of

vaporization. Sefiane and Bennacer [18] found a reduction in the evaporation rate of ethanol based aluminum nanofluid droplet on a heated PTFE (Polytetrafluoroethylene) surface as compared to the base fluid. In addition, they observed that the droplet evaporation followed the  $d^2$ -law under higher convective temperature but not at lower or natural convection conditions [27]. Wei et al. [28] investigated numerically the dependence of evaporation rate on the Peclet number, particle concentration and contact angle of the droplet containing nanoparticles. Gan and Qiao [29] observed experimentally that adding MWCNT's to ethanol enhanced the evaporation rate and droplet temperature due to improved optical absorption. Information on the micro flow visualization via nanoparticle image velocimetry (nPIV) and total internal reflection microscopy (TIRFM) for velocity measurement can be consulted in the **supporting material**.

Using nanoparticles for direct absorption of solar energy in a working fluid is a recent development [30-38]. Most of the work is at the macro scale in which either the nanoparticle assisted fluid heating [32, 33, 37, 38] or steam generation [30, 35, 36] were investigated under various radiation conditions by studying the space and/or temporal temperature variation over the time. However, the information regarding heat transfer, fluid flow, particle velocity and subsequent dry patterns at the micro droplet level is still lacking in the literature. This work proposed a novel experimental study to reveal the real time motion of fluorescent particles in a droplet of nanofluid near the three phase contact line by using TIRFM and MnPIV techniques [39]. The radiation absorptivity of Si/Ag hybrid nanoparticles at the micro droplet level is studied under different radiation fluxes and the corresponding droplet evaporation rates are revealed. The deposition patterns of the nanofluid droplet after the evaporation are obtained with the help of tracer particles using TIRFM. The particle movement behavior during the droplet evaporation is further explained with the help of obtained deposition patterns.

## 2. Experimental section

### 2.1. Reagents and devices

A commercially available silicon powder (supplied by Nanostructured & Amorphous material Inc.) and silver nitrate,  $\text{AgNO}_3$  (Sigma Aldrich Co) were used to synthesize Si/Ag core/shell hybrid nanoparticles. To visualize the flow dynamics and deposition patterns under total internal reflection fluorescence microscopy (TIRFM), fluorescent polystyrene microspheres (Invitrogen FluoSphere F8803 supplied by Thermo Fisher) with 50 nm as nominal radius were used as tracer particles. Tracer particles with two concentrations of  $2.5 \times 10^{-4}$  w/v% and  $5.0 \times 10^{-4}$  w/v% were used with various concentrations of core/shell Si/Ag nanoparticles. The droplet evaporation tests were conducted on a pendant drop setup (JC2000D4M), equipped with a computer controlled high speed camera and coverslips (Thermo Fisher) were used as substrate.

### 2.2. Nanoparticle synthesis

The synthesis of Si/Ag core/shell hybrid nanoparticles was completed in two phases. The first phase included the dispersion of Si nanopowder with a particle size between 40 nm and 100 nm. The second step in the core-shell fabrication process was to coat the Si nanoparticles with Ag through solution impregnation technique. This is a modified methodology developed by Kumar and Raza [40] where 1 g of Si powder was dispersed with 100 ml of 0.25 M  $\text{AgNO}_3$  (as a source of Ag NPs) under vigorous stirring. To complete the solution impregnation process, the mixture was allowed for at least 36 hours stirring at room temperature. The solution was then calcined in a muffle furnace at 700 °C for 2 hours. A light grey powder was obtained which was re-dispersed in de-ionized water to get a measured concentration. The hybrids of the tracer particle solution as

base fluid and Si/Ag nanofluid were made by mixing the known concentration of each and presented in **Table 1** in which B and H stand for base fluid and hybrid fluid respectively.

For morphological analysis on transmission electron microscope (TEM), holey Au grids were used where a drop of the core/shell Si/Ag hybrid nanofluid was dried on shiny side of grid before further analysis. TEM analysis in **Fig. 1** clearly shows that Si nanoparticles are coated with Ag. The inner dark round area in red circle in Fig. 1 (b) is the Si core while the light cloud in blue circle around the dark core is coating of silver.

### 2.3. Experimental setup and procedure

The velocity of the tracer particles near the three phase contact line of the droplet was measured using an inverted microscope (Olympus, IX71) and MnPIV technique. The fluorescent particles in hybrid with Si/Ag nanoparticles were illuminated by an evanescent wave having exponentially decaying intensity along the distance normal to the wall. An evanescent wave can be developed when a light beam travelling through a medium having refractive index  $n_1$  enters another medium having a lower refractive index  $n_2$  at angle larger than the critical angle. The critical angle ( $\theta_c$ ) can be defined as below;

$$\theta_c = \sin^{-1} \frac{n_2}{n_1} \quad (1)$$

The intensity of the evanescent wave can be expressed as below [41];

$$I(z) = I_m e^{\left(\frac{-z}{z_p}\right)} \quad (2)$$

Where  $I$  and  $I_m$  are the evanescent wave intensity and the maximum intensity at the wall (i.e.  $z = 0$ ) respectively and  $z$  and  $z_p$  are the distance normal to the wall and the penetration depth respectively. The penetration depth ( $z_p$ ) can be expressed as in Eq. (2);

$$z_p = \frac{\lambda_o}{4\pi n_1} \left[ \sin^2 \theta - \left( \frac{n_2}{n_1} \right)^2 \right]^{-\frac{1}{2}} \quad (3)$$

Where  $\lambda_o$  is the wavelength of the incident light,  $\theta$  is the incident angle. The glass coverslips (Thermo Fisher) treated with piranha solution (3:1 volume ratio of 98%  $\text{H}_2\text{SO}_4$  and 30%  $\text{H}_2\text{O}_2$ ) to make them highly hydrophilic as described in [23] were used as substrate. For the case of near wall motion analysis of the tracer particles in the nanoparticle hybrid droplet and their subsequent dry patterns, the ambient temperature and relative humidity were maintained at  $22 \pm 1$  °C and  $40 \pm 1\%$  respectively.

The evanescent illumination was obtained from a continuous wave solid laser (Coherent, FV5-LA-AR) coupled with an optical fiber at a wavelength of 488 nm. A penetration depth ( $z_p$ ) of 86 nm was achieved by a total internal reflection fluorescence (TIRF) objective lens having magnification of 60x. The optical fiber had a coupling efficiency of about 65% and the laser output power was  $>5$  mW. An epifluorescent bandpass filter cube (Chroma Tech, HQ550/40 m) isolates the polystyrene emissions. The bandpass filter transmits light at 512 nm wavelength and reflects the 488 nm radiance which is imaged by the TIRF objective at 15 mS exposure time on to EMCCD (Electron multiplying charge coupled device, Andor, IXON 3 Ultra). The EMCCD recorded 16 bit  $256 \times 256$  pixels images at an electronic gain of 8 and framing rate of about 62 Hz. The imaging system with 60x magnification has field view of  $68.26 \times 68.26 \mu\text{m}^2$ . The excitation light with a very small intensity (5mW) has a negligible influence on the droplet evaporation which was also confirmed by recording the total drying time with and without excitation light under the same ambient conditions. A schematic of the TIFRM setup is given in **Fig. 2 (a)** and a photo of the inverted microscope is given in **Figure S1 in the supporting data**.

The experimental procedure includes the steps: (i) lubricating the TIRFM objective lens with appropriate volume of immersion oil, (ii) placing the prepared glass coverslip (substrate) on the TIRFM objective, (iii) dripping a drop 0.5  $\mu\text{L}$  of nanofluid with a precise micropipette (Fisher Scientific) on the substrate, (iv) adjusting the objective lens to bring the bottommost part of the droplet in focus, (v) adjusting the incident angle of the excitation light for the generation of an evanescent wave at the lowermost part of the substrate for total internal reflection and bringing the objective lens in perfect focus, (vi) recording the particle motion information through EMCCD with an interval of 10 second till the complete evaporation of the droplet, (vii) image processing using standard algorithm of particle velocimetry and (viii) changing the nanofluid concentration by following the steps (ii) through (vii). A schematic of the experimental procedure for flow analysis is also shown in **Fig. 3**. In one measurement, the EMCCD recorded a series 100 images with 50 sets of in-plane intensity data which were averaged to minimize the chance random error.

The tracer particle position with respect to the wall and thus the movement of the tracer particles in the liquid film close to the three phase line can be quantified by processing the images using standard algorithm of particle velocimetry. The technique and its accuracy had already been validated by various researchers [21, 41-43] using different methods including micro scale Poiseuille flow, near wall flow, nanoscale near wall contact line visualization and electro osmotic flow. The uncertainty in the velocity can be reduced to <4% by carefully choosing the size of measuring window, time interval and averaging multiple results as suggested by R. Sadr et al. [44].

The evaporation of the nanofluid droplet containing Si/Ag nanoparticles and fluorescent tracer particles was carried out on a pendant drop setup (JC2000D4M) under different irradiance levels

as schematically shown in **Fig. 2 (b)**. The droplet drying process was imaged with a high speed CCD camera at the rate of 25 frames per second. The spatial resolution of the imaging system was about 3  $\mu\text{m}$  per pixel. The distance between the imaging system and the droplet was kept constant to have comparable results. A micro syringe pump was used to drip the droplet on the glass substrate. The droplet was evaporated three times under each radiation condition to confirm the consistency in the drying time recording. Images were taken from the time of dripping the droplet onto the glass substrate till it vanished completely. A self-developed MATLAB code was used to process all the images which counts the number of pixels in the droplet zone. The pixels could be converted to droplet nominal diameter, droplet height and volume at different time intervals during the evaporation by scaling the pixels to an object of known size. The deposition patterns of the dried droplet in each case were recorded on TIRFM setup using laser light and 10x magnification objective with EMCCD.

### 3. Results and analysis

#### 3.1. Near-wall tracer particle motion analysis

The measurement of in-plane average velocity of tracer particles near the three phase line of the nanofluid droplet was done using MnPIV technique from the series of images recorded through EMCCD. The average in-plane near wall velocity of tracer particles dispersed in deionized water without nanoparticles is shown in **Fig. 4 (a)** and the velocity of tracer particles in hybrid with Si/Ag core/shell nanoparticles at various concentrations is given in **Fig. 4 (b)**. The flow behavior of the tracer particles within the droplet could be influenced by either Marangoni convection or capillary convection. As there is no externally applied heat source on the droplet area, the temperature difference developed on the basis of natural evaporation only is not enough to

develop a Marangoni effect [13]. Hence the capillary flow is thought to be the main cause of tracer particles near the three phase line of the droplet, which is also supported by the ring like deposition pattern of the droplet after evaporation as shown in **Fig. (5)**. Via particle movement analysis through TIRFM objective lens of the inverted microscope, it was observed that the outward velocity of tracer particles from the central part of the droplet was increased as they approach the contact line. This phenomenon can be attributed to a much higher evaporation rate near the three phase contact line of the droplet than at the central portion. Consequently a compensatory fluid flow from the center to the edge of the droplet is induced. This non-uniform evaporation rate of the droplet along the radial direction can be described quantitatively by taking the average in-plan tracer particle velocity and the wettability close to the edge of the droplet into account [45] and is given as below;

$$v_{avg} = (r_o - r)^{-b} \quad (4)$$

Where  $r$  is the distance between the position of the tracer particle and the center of the droplet,  $r_o$  is the initial radius of the droplet and the constant  $b$  can be expressed as below;

$$b = \frac{\pi - 2\theta_a}{2\pi - 2\theta_a} \quad (5)$$

where  $\theta_a$  is the contact angle of the droplet with the substrate.

It was also observed while looking through TIRFM objective lens illuminated by an evanescent wave that the tracer particle motion is complicated at the early stage of the droplet evaporation. The overall motion of the particles at the initial evaporation phase was such that the tracer particles were moving towards the center of the droplet in lower sublayers and towards the droplet edge in the upper sublayers indicating a compensatory circulating flow towards the three

phase contact line region. The particle motion at the lower sublayers of the droplet was suppressed at the final evaporation phase and the velocities of the tracer particles from the center to the droplet edge increased continuously as shown in **Fig 4**, irrespective of the concentration of the tracer particles and nanoparticles. A slight decrease in the particle velocity was observed at the last moment of evaporation of droplet having no Si/Ag nanoparticles (B1 and B2) as shown in **Fig. 4 (a)**. But no such suppression in velocity was observed for the droplets having Si/Ag nanoparticles in hybrid with the tracer particles (H1 through H4) as shown in **Fig. 4 (b)**, which can be associated to a relatively rapid evaporation rate at the final evaporation phase.

The velocity profiles of the tracer particle in the droplet as given in **Fig. 4 (b)** show that the near wall velocity in the droplet having less concentration of Si/Ag nanoparticles is higher than that of higher concentration at a given tracer particle concentration. Also the motion of the tracer particle is suppressed close to the three phase contact line as the concentration of the fluorescent particles or Si/Ag nanoparticle is increased. This might be associated with the increased particle density and the inter-particle collisions, which may suppress the movement of the particles in the droplet during evaporation.

The deposition patterns of the droplet dried under the ambient conditions and in the absence of any external heat source are shown in **Fig. 5**. The evaporation of the sessile droplet may follow the constant contact radius (CCR) mode or the constant contact angle (CCA) mode or combination of them. In CCR mode, the contact line of the droplet is pinned to the substrate and the contact angle keeps on decreasing while the contact angle remains fixed and the droplet contact area keeps decreasing during the evaporation in CCA mode [46]. The evaporation of the droplets in the current study followed the CCR mode during the initial evaporation phase while the CCA mode was followed at the dry out phase of the droplet as shown in **Fig. 5**, which is in-

line with the observation from a few other researchers [28, 47-49]. Fig. 5 also shows that both tracer particle concentration and nanoparticle concentration affect the drying patterns significantly. In the absence of nanoparticles, more tracer particles are accumulated toward the droplet center as the evaporation proceeds. A clearly distinct multi ring structured dry pattern of the evaporated droplet is developed at the lower concentration of the tracers, showing a stick-slip flow behavior. A higher concentration of tracers develops radial spokes in combination with tightly packed concentric multi rings, as also mentioned by Sun et al. [23]. With the inclusion of nanoparticles, the inward movement of tracer particles was retarded, as suggested by a nearly zero tracer particle concentration at the center of the droplet after drying. Instead high concentrations of tracer particles are seen in outer rings, which suggests that during CCA mode, the presence of nanoparticles retarded the inward movement of the contact line and increased the pinning time, drawing the surrounding tracer particles to the contact line.

### 3.2. Droplet evaporation and deposition patterns

The evaporation profiles of the droplets for various concentrations of the fluorescent particles and core/shell Si/Ag nanoparticles under varying irradiance levels are given in **Fig. 7** and **Fig. 8**. There was a slight variation in the initial droplet volume in each experiment, normalized volume ( $V_n$ ) during the droplet evaporation time are compared which can be calculated as below;

$$V_n = \frac{V_t}{V_0} \quad (6)$$

Here  $V_t$  is the droplet volume at any time  $t$  during the evaporation and  $V_0$  is the initial droplet volume. As the normalized volume is a ratio of the volumes, it does not have any unit. **Figure S2** in supporting material shows the evaporation of the droplet containing tracer particles only (B1 and B2) and act as a baseline for the hybrid droplet evaporation. **Figure S2 (a)** shows that the

tracer particles have negligible influence on the evaporation of the droplet. As the tracer particles are the fluorescent particles only (i.e. with very weak light absorptivity), the change in the intensity of light as a heat source has almost no influence on the droplet evaporation behaviour. **Figure S2 (b)** shows that evaporation curves for the three irradiance levels almost overlap each other at the initial stage of the evaporation. The final stage of the droplet evaporation experiences a very negligible effect of incoming light intensity. It can be assumed that any significant change in the evaporation behaviour of the droplet is due to the core/shell Si/Ag nanoparticles.

The normalized evaporated volume over the evaporation time for the droplet from hybrid H1 under the varied incoming heat fluxes is given in **Fig. 6**. The presence of Si/Ag core/shell nanoparticles in the droplet changed the evaporation time of the droplet dramatically under different irradiance levels. The light absorbing Si/Ag nanoparticles decreased the evaporation time of the droplet as the intensity of the incoming light is increased thereby increasing the evaporation rate as shown in the inset of **Fig. 6**. The evaporation rate is increased from 5.8  $\mu\text{L/s}$  to 10.6  $\mu\text{L/s}$  as the irradiance is increased from ambient to 75 W for the same amount of tracer particles and nanoparticles. This increase in the droplet evaporation rate can be associated with the localized heating around the highly absorbing nanoparticles. **Fig. 7 (a)** shows the influence of Si/Ag nanoparticle concentration in hybrids H1 and H3 compared with B1 at 75 W irradiance while the effect of core/shell nanoparticles in hybrids H2 and H4 compared with their respective base fluid B2 under 25 W is presented in **Fig. 7 (b)**. The droplet evaporation rate is increased from 9  $\mu\text{L/s}$  to 14  $\mu\text{L/s}$  with the addition of only 0.006 w% Si/Ag nanoparticles, i.e., an enhancement of 55.5% over the base fluid.

The fluid flow dynamics and the effect of nanoparticle addition on the three phase contact line pinning during the droplet evaporation can also be observed from the deposition patterns. The

particles in the droplets having different particle concentrations and evaporated under varied irradiance levels exhibited different deposition patterns as can be seen in **Fig. 8** and **Fig. 9**.

Similar to the non-irradiation case, a non-uniform evaporation caused by the capillary flow takes most of the particles in the droplet to the contact line and deposited there. Consequently a bright ring is developed as shown in **Fig. 8**. It can be stated that the very first pinning-depinning-pinning cycle of the droplet contact line during almost half of the droplet evaporation time is wider for the lower particle concentrations than that of higher concentrations of the tracers as well as Si/Ag nanoparticles. Then the recurring process of pinning and depinning of the droplet contact line which is also known as ‘stick-slip behavior’ starts till the complete evaporation of the droplet thereby giving a multi-ring like pattern of the dried droplet. In some cases, the contact line is pinned and the residual fluid at the center of the droplet is moved to the pinned edge under thermocapillary flow at the final evaporation stage of the droplet, leaving a relatively empty space at the center of the droplet as shown in **Fig 8 (c)** and **Fig. 9 (b and c)**. The recurring rate of stick-slip of the contact line of droplet having higher particle loading and under the higher thermal intensity is so fast that the overlapping or in some cases very tightly packed asymmetric rings pattern is developed during the droplet evaporation as can be seen in **Fig. 9**.

The particle velocity, evaporation rate and deposition patterns of the droplet are significantly influenced by the concentration of the Si/Ag core/shell nanoparticles, tracer particles and radiation intensity. The concentration of the nanoparticles greatly enhanced the droplet evaporation rate due to the highly absorbing Si/Ag nanoparticle, which also influence the deposition patterns. However the mechanism of asymmetrically deposited particles duration the evaporation of the droplets containing tracer particle and Si/Ag nanoparticle hybrids is a complex phenomenon and required further detailed study.

#### 4. Conclusion

The near wall particle motion, evaporation rate and deposition patterns of sessile droplets containing a hybrid of tracer particles and core/shell Si/Ag nanoparticles are investigated experimentally in this paper. This is an advancement in the preliminary studies [21, 23] on the near-wall fluorescent particle motion in a sessile droplet evaporation. Unlike the numerous numerical [50, 51] or experimental and/or numerical [11, 27, 52, 53] studies, which individually focused either fluid flow, heat transfer characteristics, evaporation modes or dry patterns of only one type of nanofluid droplet, this study presents a detailed experimental insight into the effects of these factors in an evaporating Si/Ag nanofluid droplet and their influences on the consequential deposition pattern. It was observed that the tracer particle motion, determined by the MnPIV technique, exhibited a circling pattern at the initial evaporation stage due to the non-uniform evaporation rates between the edge and the center of the droplet. An enhancement of about 55.5% in the droplet evaporation rate was observed with only 0.006 wt% concentration of Si/Ag nanoparticles. The pinning and depinning of the contact line of the droplet and the pinning time were significantly influenced by the concentration of the nanoparticles, which also altered the deposition pattern of the tracer particles. The constant contact radius (CCR) and constant contact angle (CCA) modes of the droplet evaporation were followed recurrently during the evaporation process, which is consistent with the observation of some other researchers [28, 47-49], giving rise to asymmetrical deposition patterns. The nanoparticle concentration significantly influenced the droplet evaporation rate, leading to an irregular deposition patterns. The addition of radiation-sensitive Si/Ag composite nanoparticles in the droplets may be a very important feature in spray drying and thin film coating on which the future work will be focused.

**Acknowledgement**

The authors acknowledge the financial support from University of Engineering and Technology (UET) Lahore in collaboration with HEC (Higher Education Commission) Pakistan under FDP, the National Science Foundation of China (Grant No. 51228601) and British Council Newton Fund-PhD Placement Grant (Grant No. 473117) for this research. The authors also acknowledge the support of Prof. M. Yoda's group at Georgia Tech, USA for developing the MnPIV code used for near-wall velocity calculation.

## References

1. Wu, J., et al., Inkjet-printed microelectrodes on PDMS as biosensors for functionalized microfluidic systems. *Lab on a Chip - Miniaturisation for Chemistry and Biology*, 2015. **15**(3): p. 690-695.
2. Choi, Y., J. Han, and C. Kim, Pattern formation in drying of particle-laden sessile drops of polymer solutions on solid substrates. *Korean Journal of Chemical Engineering*, 2011. **28**(11): p. 2130-2136.
3. Grouchko, M., A. Kamyshny, and S. Magdassi, Formation of air-stable copper-silver core-shell nanoparticles for inkjet printing. *Journal of Materials Chemistry*, 2009. **19**(19): p. 3057-3062.
4. Calvert, P., Inkjet printing for materials and devices. *Chemistry of Materials*, 2001. **13**(10): p. 3299-3305.
5. Sefiane, K., On the Formation of Regular Patterns from Drying Droplets and Their Potential Use for Bio-Medical Applications. *Journal of Bionic Engineering*, 2010. **7**, **Supplement**: p. S82-S93.
6. Sobac, B. and D. Brutin, Desiccation of a sessile drop of blood: Cracks, folds formation and delamination. *Colloids and Surfaces A: Physicochemical and Engineering Aspects*, 2014. **448**: p. 34-44.
7. Fang, X., et al., Drying of DNA droplets. *Langmuir*, 2006. **22**(14): p. 6308-6312.
8. Majumder, M., et al., Overcoming the "coffee-stain" effect by compositional Marangoni-flow-assisted drop-drying. *J Phys Chem B*, 2012. **116**(22): p. 6536-42.
9. Ward, C.A. and F. Duan, Turbulent transition of thermocapillary flow induced by water evaporation. *Physical Review E*, 2004. **69**(5): p. 056308.
10. Zhong, X. and F. Duan, Flow regime and deposition pattern of evaporating binary mixture droplet suspended with particles. *The European Physical Journal E*, 2016. **39**(2): p. 1-6.
11. Park, C.-S., H. Kim, and H.-C. Lim, Study of internal flow and evaporation characteristics inside a water droplet on a vertically vibrating hydrophobic surface. *Experimental Thermal and Fluid Science*, 2016. **78**: p. 112-123.
12. Sempels, W., et al., Auto-production of biosurfactants reverses the coffee ring effect in a bacterial system. *Nat Commun*, 2013. **4**: p. 1757.
13. Deegan, R.D., et al., Capillary flow as the cause of ring stains from dried liquid drops. *Nature*, 1997. **389**(6653): p. 827-829.
14. Uchiyama, H., D. Shimaoka, and H. Kozuka, Spontaneous pattern formation based on the coffee-ring effect for organic-inorganic hybrid films prepared by dip-coating: effects of temperature during deposition. *Soft Matter*, 2012. **8**(44): p. 11318-11322.
15. Hu, H. and R.G. Larson, Marangoni Effect Reverses Coffee-Ring Depositions. *The Journal of Physical Chemistry B*, 2006. **110**(14): p. 7090-7094.
16. Gan, Y. and L. Qiao, Radiation-enhanced evaporation of ethanol fuel containing suspended metal nanoparticles. *International Journal of Heat and Mass Transfer*, 2012. **55**(21-22): p. 5777-5782.
17. Chen, R.-H., T.X. Phuoc, and D. Martello, Effects of nanoparticles on nanofluid droplet evaporation. *International Journal of Heat and Mass Transfer*, 2010. **53**(19-20): p. 3677-3682.
18. Sefiane, K. and R. Bennacer, Nanofluids droplets evaporation kinetics and wetting dynamics on rough heated substrates. *Advances in Colloid and Interface Science*, 2009. **147-148**: p. 263-271.
19. Cui, L., et al., Avoiding coffee ring structure based on hydrophobic silicon pillar arrays during single-drop evaporation. *Soft Matter*, 2012. **8**(40): p. 10448-10456.
20. Dou, R. and B. Derby, Formation of coffee stains on porous surfaces. *Langmuir*, 2012. **28**(12): p. 5331-8.
21. Xiao, C., et al., Near-wall fluid flow near the pinned contact line during droplet evaporation. *Experimental Thermal and Fluid Science*, 2016. **72**: p. 210-217.
22. Chen, C.-T., F.-G. Tseng, and C.-C. Chieng, Evaporation evolution of volatile liquid droplets in nanoliter wells. *Sensors and Actuators A: Physical*, 2006. **130-131**: p. 12-19.

23. Sun, Z., et al., Nanoparticle motion and deposition near the triple line in evaporating sessile water droplet on a superhydrophilic substrate. *Experimental Thermal and Fluid Science*, 2016. **76**: p. 67-74.
24. Van Nguyen Truskett, K.J.S., Influence of Surfactants on an Evaporating Drop: Fluorescence Images and Particle Deposition Patterns. *Langmuir*, 2003. **19**: p. 8271-8279.
25. Leonid V. Govor, G.H.B., Gu'nter Reiter, Elena Shevchenko, Horst Weller, and Ju'rgen Parisi, Self-Assembly of CoPt<sub>3</sub> Nanoparticle Rings Based on Phase-Separated Hexadecylamine Droplet Structure. *Langmuir*, 2003. **19**: p. 9573-9576.
26. Still, T., P.J. Yunker, and A.G. Yodh, Surfactant-Induced Marangoni Eddies Alter the Coffee-Rings of Evaporating Colloidal Drops. *Langmuir*, 2012. **28**(11): p. 4984-4988.
27. Gan, Y. and L. Qiao, Evaporation characteristics of fuel droplets with the addition of nanoparticles under natural and forced convections. *International Journal of Heat and Mass Transfer*, 2011. **54**(23-24): p. 4913-4922.
28. Wei, Y., W. Deng, and R.-H. Chen, Effects of insoluble nano-particles on nanofluid droplet evaporation. *International Journal of Heat and Mass Transfer*, 2016. **97**: p. 725-734.
29. Gan, Y. and L. Qiao, Optical Properties and Radiation-Enhanced Evaporation of Nanofluid Fuels Containing Carbon-Based Nanostructures. *Energy & Fuels*, 2012. **26**(7): p. 4224-4230.
30. Jin, H., et al., Steam generation in a nanoparticle-based solar receiver. *Nano Energy*, 2016. **28**: p. 397-406.
31. Lukianova-Hleb, E., et al., Plasmonic Nanobubbles as Transient Vapor Nanobubbles Generated around Plasmonic Nanoparticles. *ACS Nano*, 2010. **4**(4): p. 2109-2123.
32. Govorov, A.O. and H.H. Richardson, Generating heat with metal nanoparticles. *Nano Today*, 2007. **2**(1): p. 30-38.
33. Zhang, H., et al., Dependence of Photothermal Conversion Characteristics on Different Nanoparticle Dispersions. *Journal of Nanoscience and Nanotechnology*, 2015. **15**(4): p. 3055-3060.
34. Zhang, H., et al., Photothermal conversion characteristics of gold nanoparticle dispersions. *Solar Energy*, 2014. **100**: p. 141-147.
35. Neumann, O., et al., Solar vapor generation enabled by nanoparticles. *ACS Nano*, 2013. **7**(1): p. 42-9.
36. Baffou, G., et al., Super-heating and micro-bubble generation around plasmonic nanoparticles under cw illumination. *Journal of Physical Chemistry C*, 2014. **118**(9): p. 4890-4898.
37. Bandarra Filho, E.P., et al., Experimental investigation of a silver nanoparticle-based direct absorption solar thermal system. *Energy Conversion and Management*, 2014. **84**: p. 261-267.
38. Jin, H., et al., Photothermal conversion efficiency of nanofluids: An experimental and numerical study. *Solar Energy*, 2016. **139**: p. 278-289.
39. Li, H.F. and M. Yoda, Multilayer nano-particle image velocimetry (MnPIV) in microscale Poiseuille flows. *Measurement Science and Technology*, 2008. **19**(7): p. 075402.
40. Kumar, R.V. and G. Raza, Photocatalytic disinfection of water with Ag-TiO<sub>2</sub> nanocrystalline composite. *Ionics*, 2009. **15**(5): p. 579-587.
41. Li, H., R. Sadr, and M. Yoda, Multilayer nano-particle image velocimetry. *Experiments in Fluids*, 2006. **41**(2): p. 185-194.
42. Sadr, R., et al., Diffusion-induced bias in near-wall velocimetry. *Journal of Fluid Mechanics*, 2007. **577**: p. 443-456.
43. Sadr, R., et al., An experimental study of electro-osmotic flow in rectangular microchannels. *Journal of Fluid Mechanics*, 2004. **506**: p. 357-367.
44. Sadr, R., H. Li, and M. Yoda, Impact of hindered Brownian diffusion on the accuracy of particle-image velocimetry using evanescent-wave illumination. *Experiments in Fluids*, 2005. **38**(1): p. 90-98.

45. Deegan, R.D., et al., Contact line deposits in an evaporating drop. *Physical Review E*, 2000. **62**(1): p. 756-765.
46. Picknett, R.G. and R. Bexon, The evaporation of sessile or pendant drops in still air. *Journal of Colloid and Interface Science*, 1977. **61**(2): p. 336-350.
47. Hong, S.-J., et al., Advancing and receding wetting behavior of a droplet on a narrow rectangular plane. *Colloid and Polymer Science*, 2013. **291**(2): p. 347-353.
48. Zhang, C., X. Zhu, and L. Zhou, Morphology tunable pinning force and evaporation modes of water droplets on PDMS spherical cap micron-arrays. *Chemical Physics Letters*, 2011. **508**(1-3): p. 134-138.
49. Wang, F.-C. and H.-A. Wu, Pinning and depinning mechanism of the contact line during evaporation of nano-droplets sessile on textured surfaces. *Soft Matter*, 2013. **9**(24): p. 5703-5709.
50. Diddens, C., et al., Modeling the evaporation of sessile multi-component droplets. *J Colloid Interface Sci*, 2017. **487**: p. 426-436.
51. Wang, Y., et al., Expressions for the evaporation of sessile liquid droplets incorporating the evaporative cooling effect. *J Colloid Interface Sci*, 2016. **484**: p. 291-297.
52. Zhong, X., H. Xie, and F. Duan, Deposition patterns from evaporating sessile droplets with suspended mixtures of multi-sized and multi-species hydrophilic and non-adsorbing nanoparticles. *Applied Thermal Engineering*, 2017. **111**: p. 1565-1572.
53. Gleason, K., H. Voota, and S.A. Putnam, Steady-state droplet evaporation: Contact angle influence on the evaporation efficiency. *International Journal of Heat and Mass Transfer*, 2016. **101**: p. 418-426.

### List of figure captions

Fig. 1 TEM micrograph of the core/shell Si/Ag nanoparticles.

Fig. 2 **(a)** Schematic of the TIRFM setup where 1 = nanofluid sessile droplet, 2 = glass substrate, 3 = TIRF objective, 4 = dichroic mirror, 5 = beam splitter, 6 = band pass filter, 7 = continuous wave solid laser, 8 = EMCCD camera, 9 = computer, and **(b)** A schematic of the nanofluid droplet drying setup.

Fig. 3 Experimental procedure for the analysis of particle motion near the three phase line of the droplet using TIRF setup

Fig. 4 The in-plane average velocity of tracer particles near the three phase line of the droplet of **(a)** base fluid and **(b)** composite nanofluid with different concentrations of core/shell Si/Ag nanoparticles. H1 (black) and H3 (green) contains 0.00025 w/v% tracer particles (B1) while H2 (red) and H4 (blue) contains 0.00050 w/v% tracer particles (B2)

Fig. 5 Deposition patterns of naturally evaporated droplet with different concentrations of tracer particles and Si/Ag core/shell nanoparticles in the absence of external heat source; **(a)** B1, **(b)** B2, **(c)** H1 and **(d)** H2. The deposition pattern images are intertwined from sub-images.

Fig. 6 Evaporation of the droplet containing hybrid H1 under different irradiance levels. The inset shows a relation between the droplet evaporation rate and irradiance

Fig. 7 Droplet evaporation having different concentrations of Si/Ag nanoparticles in hybrid with tracer particles concentration of **(a)** 0.00025 w/v% (B1) at 75 W irradiance and **(b)** 0.00050 w/v% (B2) at 25 W irradiance

Fig. 8 Deposition patterns of the droplet of **(a)** B1, **(b)** H1 and **(c)** H3 evaporated at 25 W irradiance

Fig. 9 Deposition patterns of the droplet of **(a)** B2, **(b)** H2 and **(c)** H4 evaporated at 75 W irradiance

### List of tables captions

Table 1 Concentration of tracer particles and Si/Ag nanoparticles in the hybrids and their initial average contact angle measurements

## List of Figures

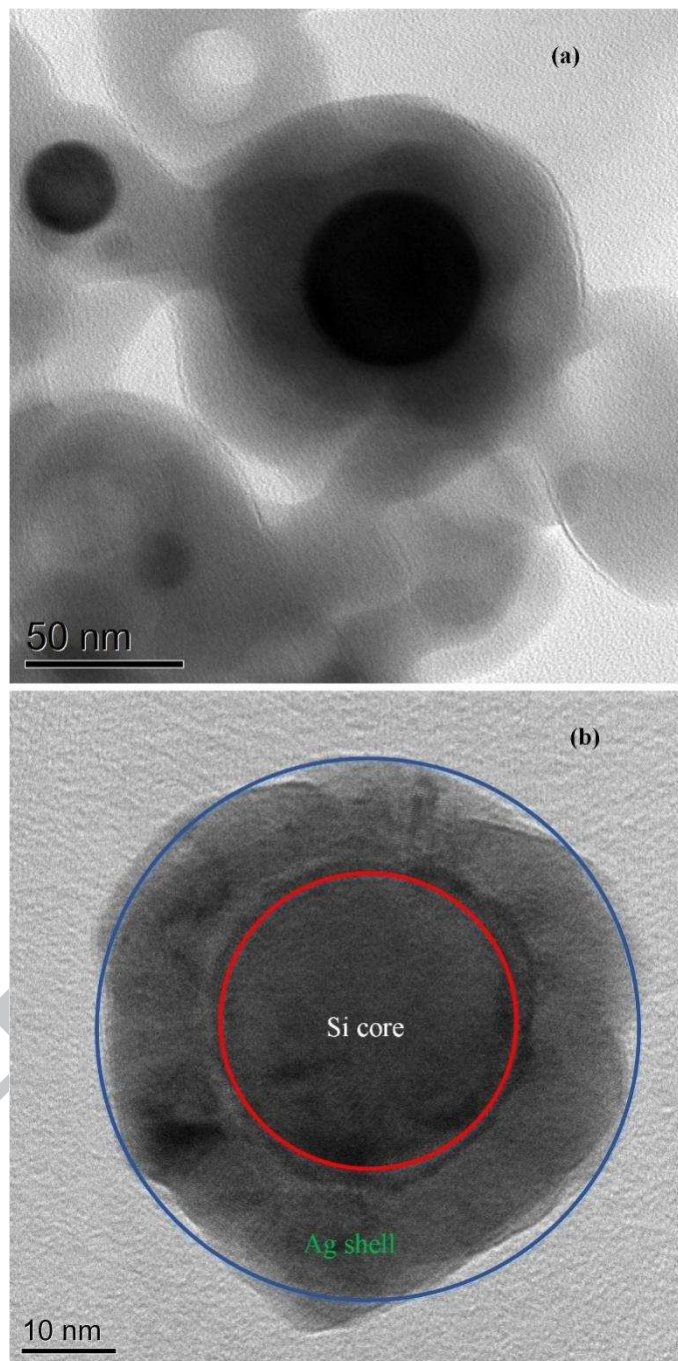


Fig. 1 TEM micrograph of the core/shell Si/Ag nanoparticles.

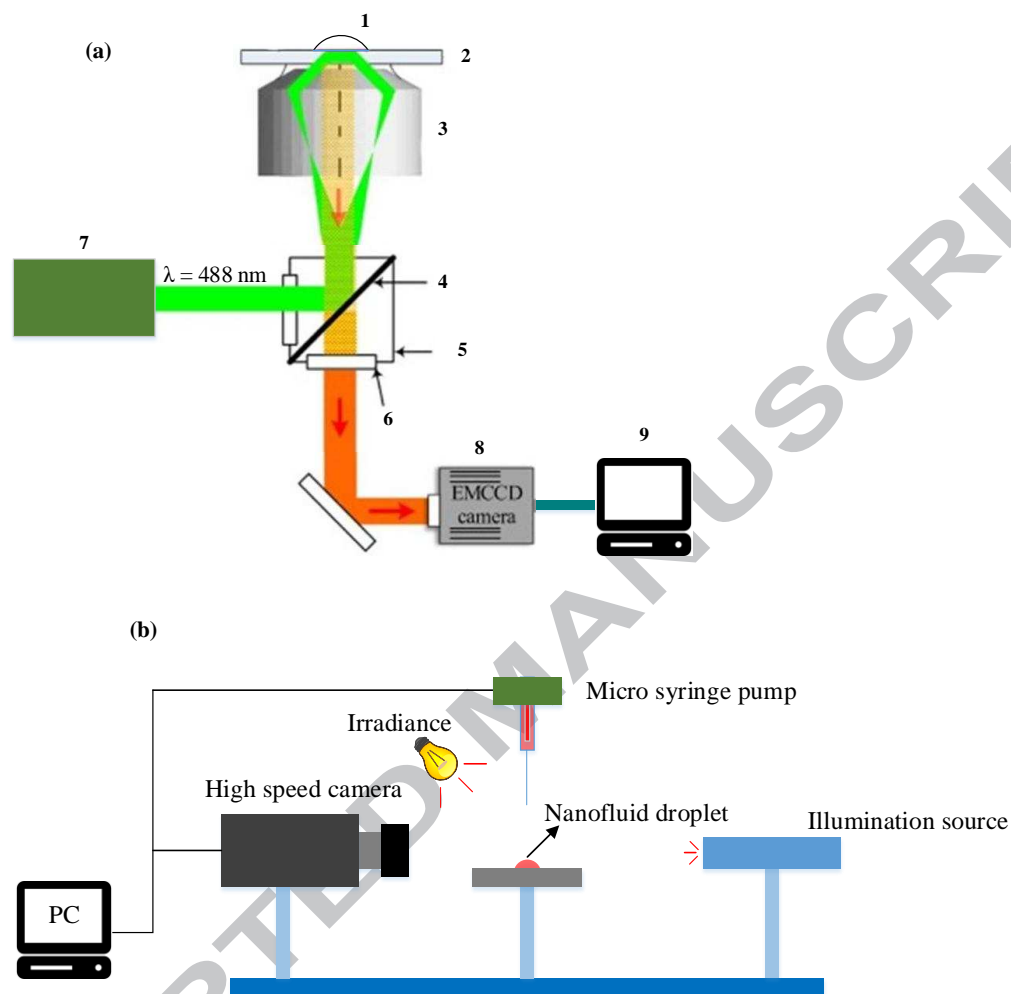


Fig. 2 (a) Schematic of the TIRFM setup where 1 = nanofluid sessile droplet, 2 = glass substrate, 3 = TIRF objective, 4 = dichroic mirror, 5 = beam splitter, 6 = band pass filter, 7 = continuous wave solid laser, 8 = EMCCD camera, 9 = computer, and (b) A schematic of the nanofluid droplet drying setup.

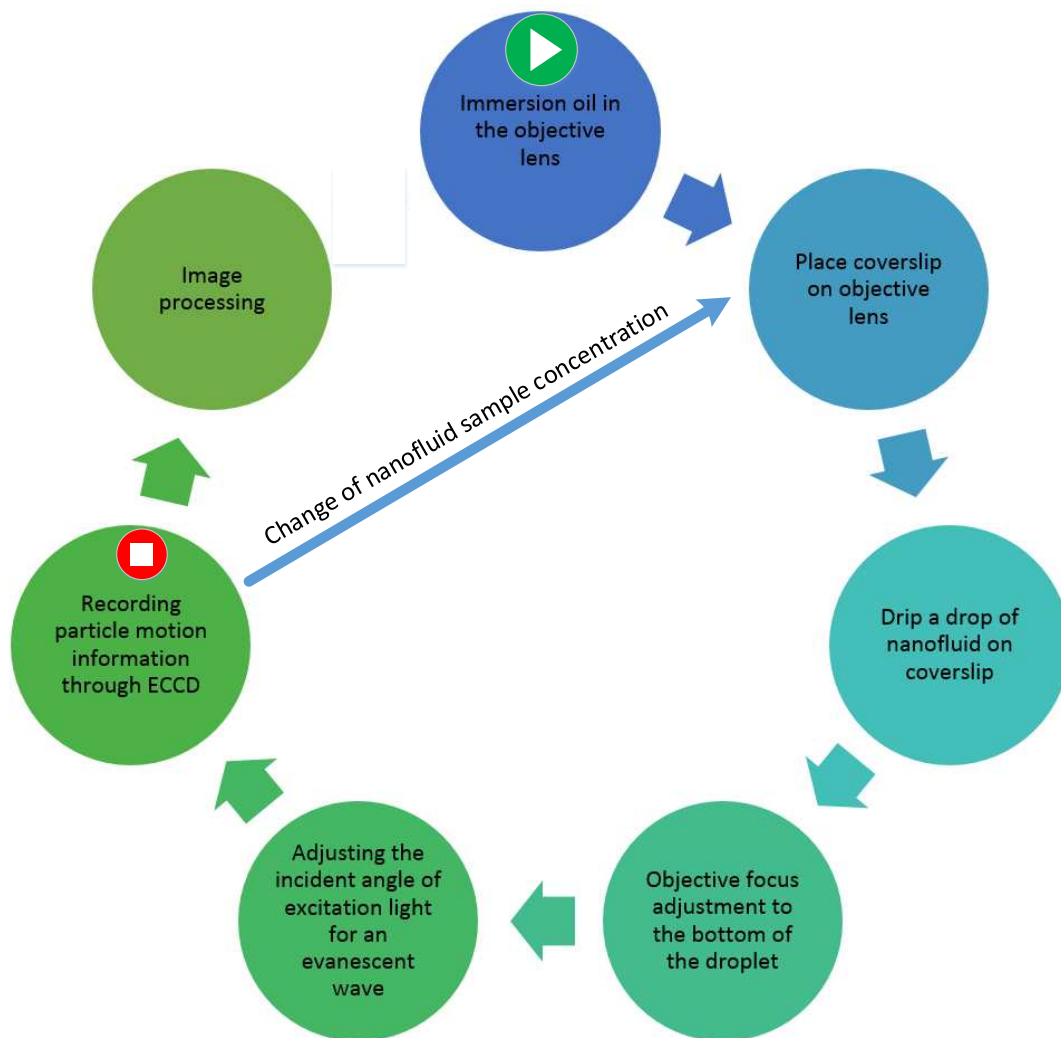


Fig. 3 Experimental procedure for the analysis of particle motion near the three phase line of the droplet using TIRF setup

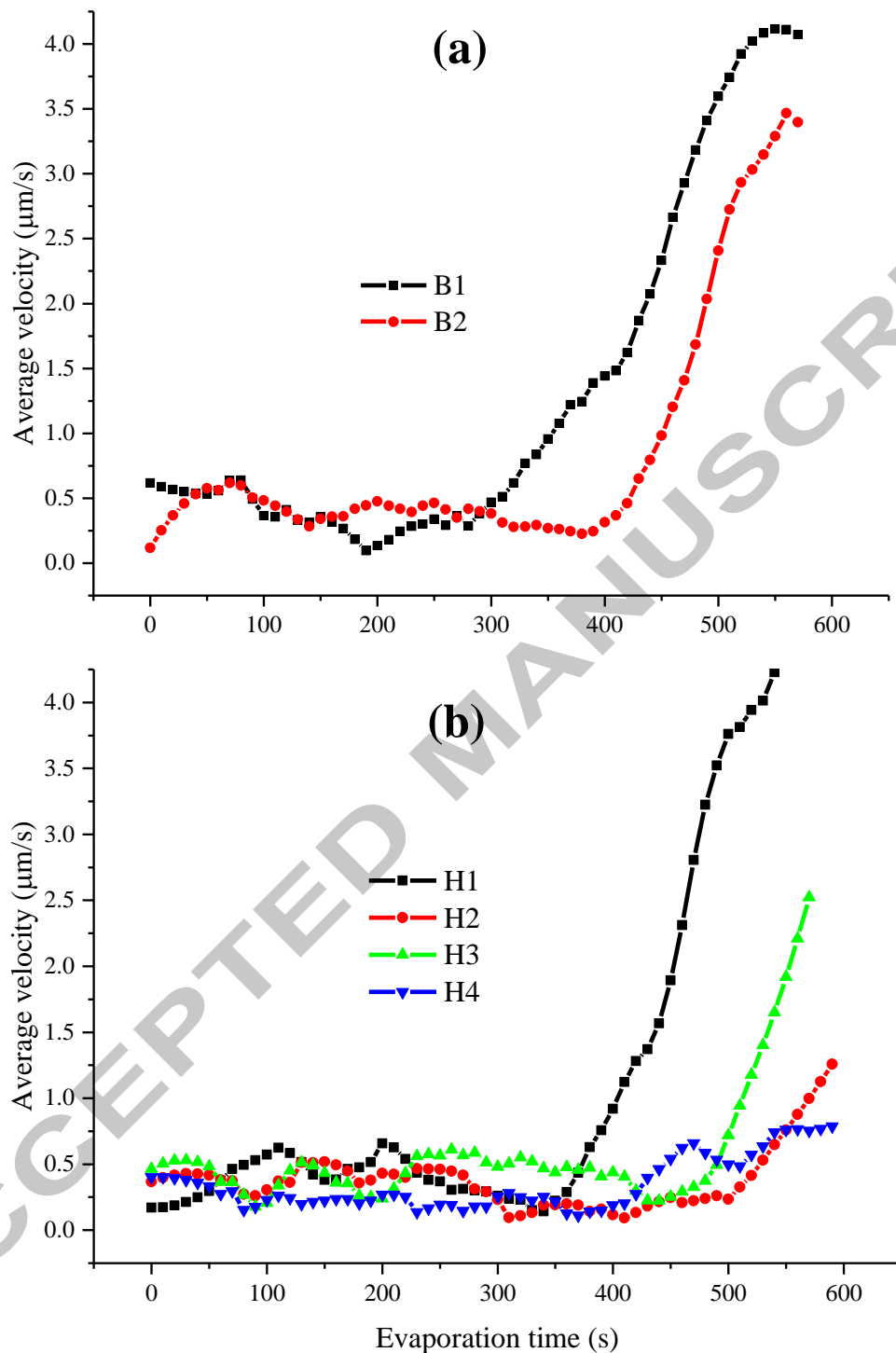


Fig. 4 The in-plane average velocity of tracer particles near the three phase line of the droplet of (a) base fluid and (b) composite nanofluid with different concentrations of core/shell Si/Ag nanoparticles. H1 (black) and H3 (green) contains 0.00025 w/v% tracer particles (B1) while H2 (red) and H4 (blue) contains 0.00050 w/v% tracer particles (B2)

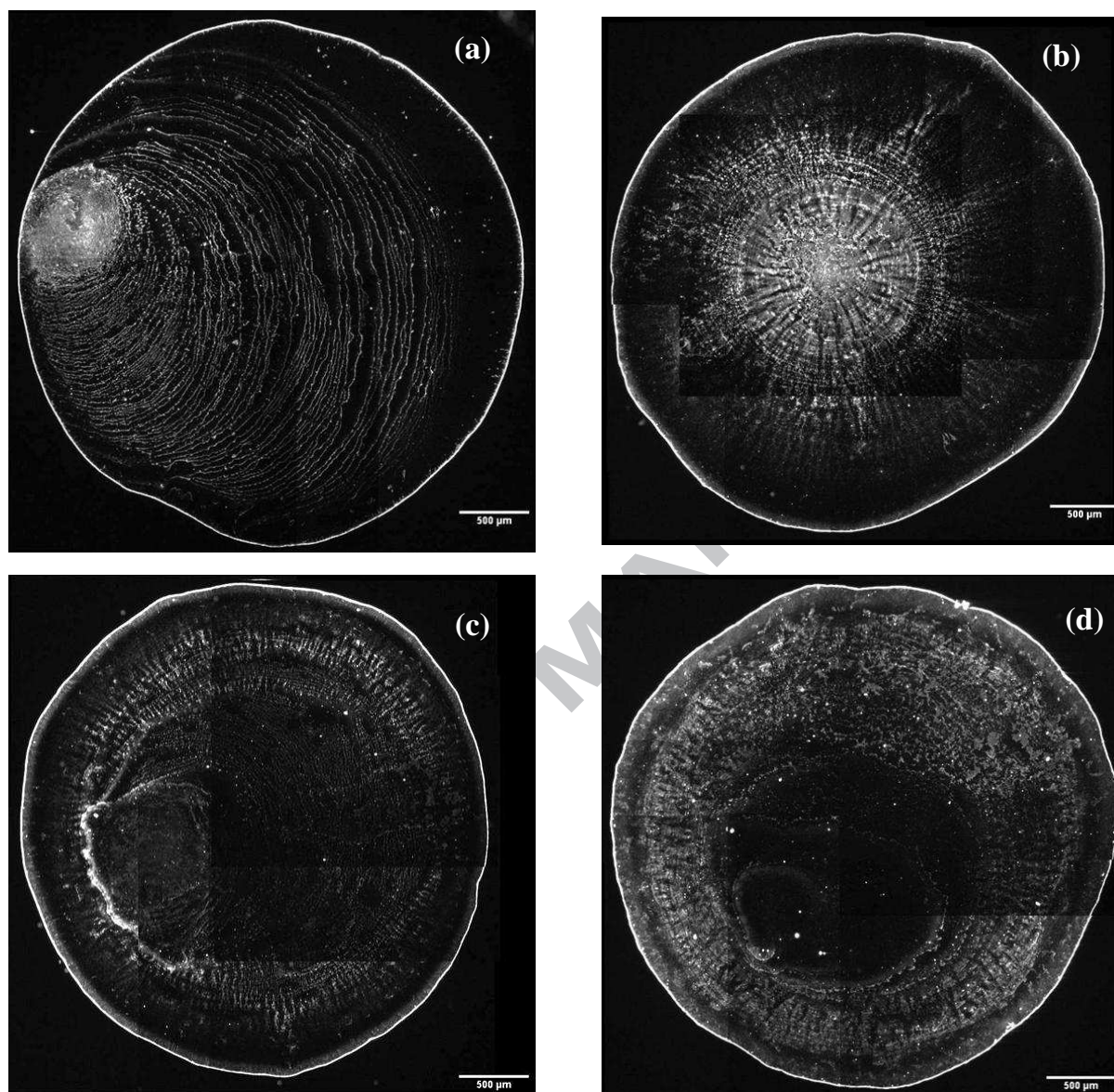


Fig. 5 Deposition patterns of naturally evaporated droplet with different concentrations of tracer particles and Si/Ag core/shell nanoparticles in the absence of external heat source; (a) B1, (b) B2, (c) H1 and (d) H2. The deposition pattern images are intertwined from sub-images.

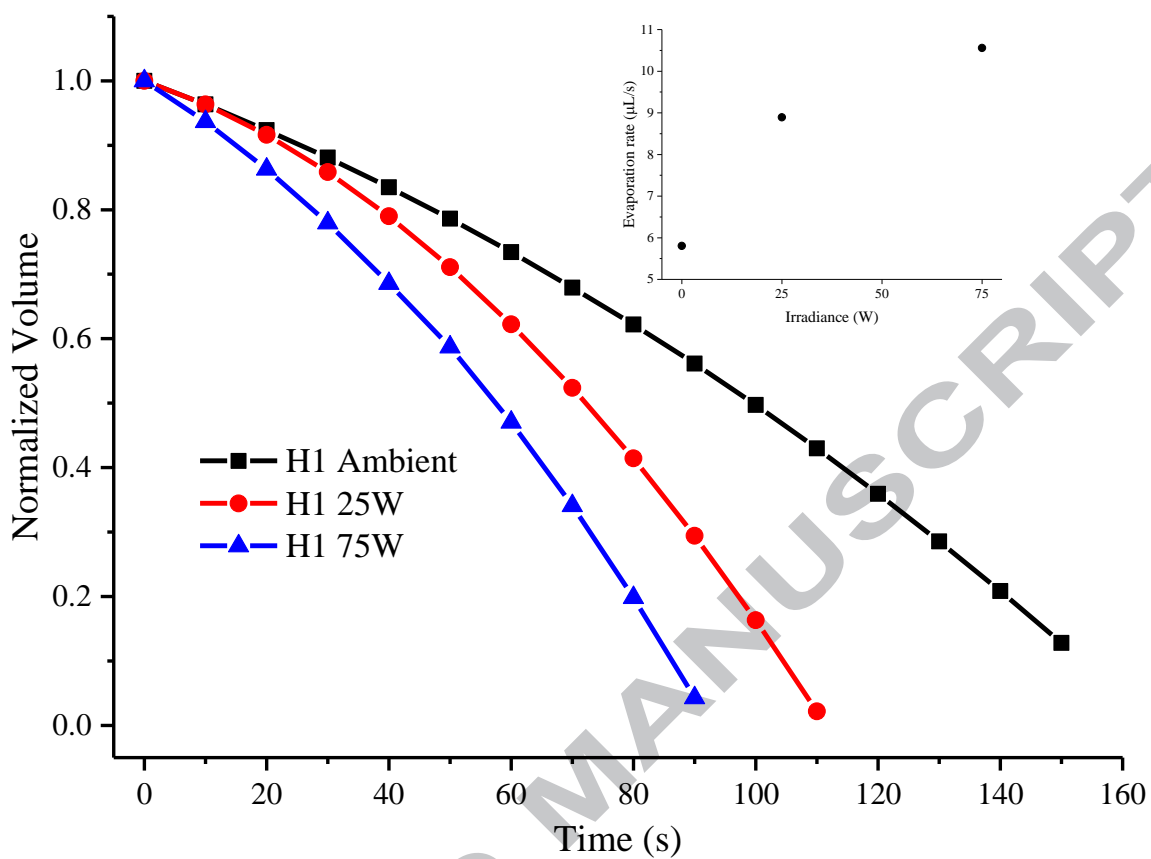


Fig. 6 Evaporation of the droplet containing hybrid H1 under different irradiance levels. The inset shows a relation between the droplet evaporation rate and irradiance

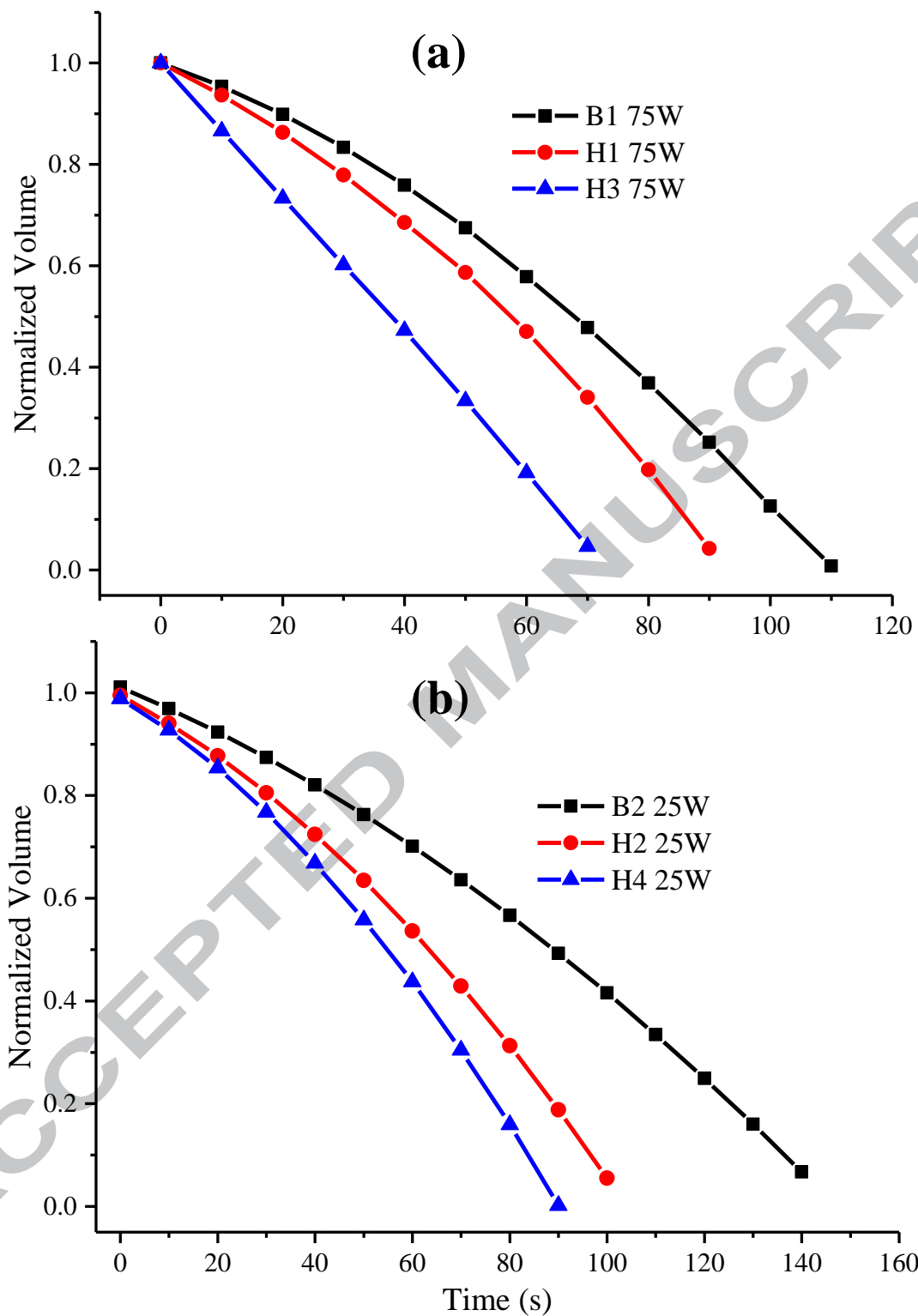


Fig. 7 Droplet evaporation having different concentrations of Si/Ag nanoparticles in hybrid with tracer particles concentration of (a) 0.00025 w/v% (B1) at 75 W irradiance and (b) 0.00050 w/v% (B2) at 25 W irradiance

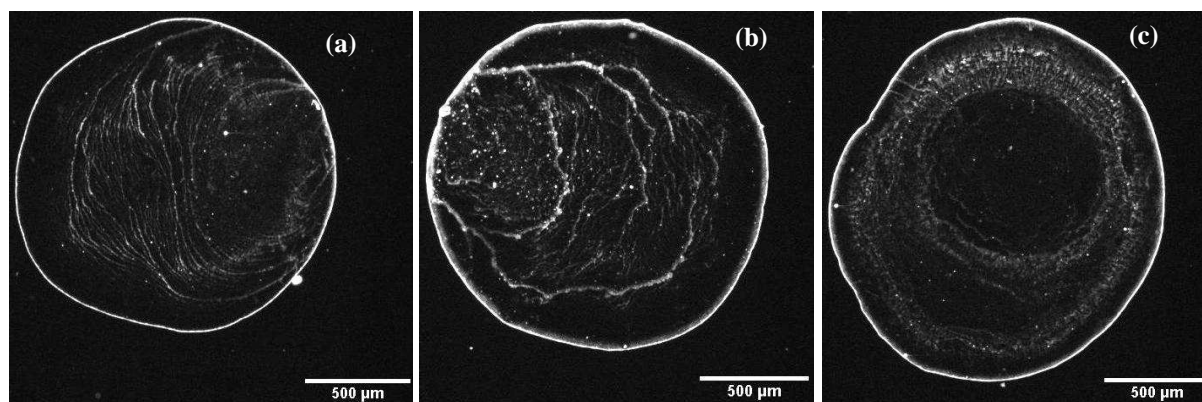


Fig. 8 Deposition patterns of the droplet of (a) B1, (b) H1 and (c) H3 evaporated at 25 W irradiance

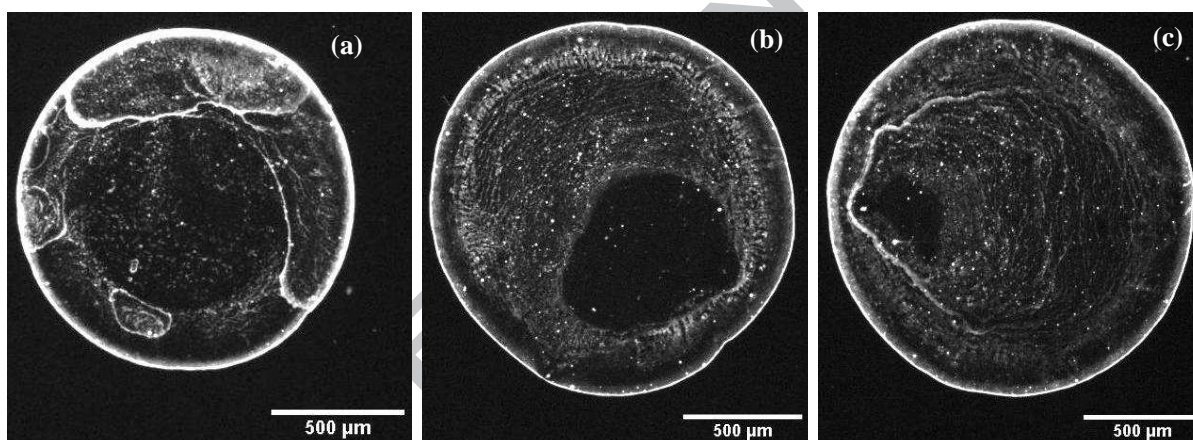


Fig. 9 Deposition patterns of the droplet of (a) B2, (b) H2 and (c) H4 evaporated at 75 W irradiance

**List of Tables**

Table 1 Concentration of tracer particles and Si/Ag nanoparticles in the hybrids and their initial average contact angle measurements

Hybrid no.	Tracer particle concentration (% w/v)	Nanoparticle concentration (% wt)	Initial contact angle (degree)
B1	0.00025	----	30.4
B2	0.00050	----	31.7
H1	0.00025	0.003	28.8
H2	0.00050	0.003	27.6
H3	0.00025	0.006	29.5
H4	0.00050	0.006	29.8